Deglacial increase of temperature variability in the tropical ocean

Lars Wörmer (lwoermer@marum.de)
MARUM, University of Bremen https://orcid.org/0000-0002-3673-3826
Jenny Wendt
MARUM, University of Bremen
Brenna Boehman
MIT-WHOI
Gerald Haug
Max Planck Institute for Chemistry
Kai-Uwe Hinrichs
University of Bremen

Physical Sciences - Article

Keywords:

Posted Date: March 16th, 2022

DOI: https://doi.org/10.21203/rs.3.rs-1317471/v1

Deglacial increase of temperature variability in the tropical ocean

Authors: Lars Wörmer[1*], Jenny Wendt[1], Brenna Boehman[1†], Gerald H. Haug[2,3], Kai-Uwe Hinrichs[1]

Affiliations:

[1]MARUM – Center for Marine Environmental Sciences and Faculty of Geosciences; University of Bremen, Bremen, Germany.

[2]Max-Planck-Institute for Chemistry; Mainz, Germany.

[3]Geological Institute, Department of Earth Sciences, ETH Zürich; Zürich, Switzerland.

*Corresponding author: lwoermer@marum.de

†Present address: MIT-WHOI Joint Program in Oceanography/Applied Ocean Science & Engineering; Cambridge and Woods Hole, MA, USA.

Abstract: The warm and relatively stable Holocene climate was preceded by a pronounced event of abrupt warming in the Northern Hemisphere, the termination of the Younger Dryas cold period[1,2]. While this transition has been intensively studied, its imprint on low latitude ocean temperature is still controversial and its effects on sub-annual to decadal climate variability remain poorly understood[1,3,4]. We applied the extraordinary resolution provided by mass spectrometry imaging of long-chain alkenones[5,6] to sediments from the tropical Cariaco Basin[7], and reveal that the seasonal amplitude of reconstructed sea surface temperature increased more than twofold during the transition into the Holocene, while average temperature was not altered. We further observe modulations in interannual sea surface temperature variability that we attribute to a muting of the El Niño-Southern Oscillation at the end of the Younger Dryas, and a subsequent intensification during the early Holocene. These dynamics are consistent with the modeled interplay of meltwater and ice sheet forcing and suggest that climate recovery in the Pacific preceded the North Atlantic Younger Dryas-Holocene transition. Our results demonstrate

that the abrupt changes that completed the most recent glacial to interglacial transition had pronounced effects on sub-and interannual climate variability in the Tropical North Atlantic.

Main Text:

The warm and relatively stable climate of the Holocene has facilitated the development of modern ecosystems, the proliferation of human societies and their cultural diversification. Its onset, however, was associated with an event of abrupt climate change. The boundary between Pleistocene and Holocene is defined by the sudden Northern Hemisphere warming that terminated the Younger Dryas (YD) cold spell[8]. The YD lasted from ~12.9 to 11.7 thousand years before AD 2000 (kyr b2k)[9] and was triggered by a reduction of the Atlantic meridional overturning circulation (AMOC) resulting from freshwater discharge at higher latitudes[10]. Its effects quickly propagated, globally affecting hydroclimate and temperature[1,2]. While correlative cooling was predominant across the Northern Hemisphere, the Southern Hemisphere, especially in the high latitudes, witnessed warming in what has been defined as the bipolar seesaw[11]. The annually laminated (varved) sediments from the Cariaco Basin, an anoxic oceanic basin located off Venezuela, have been crucial in identifying the tropical response to the YD-Holocene transition. A dry YD was succeeded by a wetter early Holocene[12], resulting in vegetation change[13]. The end of the YD also witnessed changes in primary productivity[7,14,15] and phytoplankton community composition[16]. These phenomena are explained by a northward migration of the Intertropical Convergence Zone (ITCZ), which resulted in increased precipitation, but reduced trade winds and upwelling in the area. With respect to sea surface temperature (SST), the reconstructed pattern of change in the lower latitudes is more heterogeneous, and a greater impact of the YD on the hydrological cycle than on SST is assumed[1]. In the western Tropical North Atlantic (TNA), proxy records have revealed both a slightly warmer YD, consistent with a decrease of northward heat transport[4,17], and a comparatively cool YD, as recorded by planktonic foraminifera in the Cariaco Basin[3].

These SST reconstructions record changes in mean states, averaging decades or centuries into single data points. The forcing of climate variability on seasonal to interannual scales during this and other major climatic transitions, however, remains unresolved. Perturbations on these timescales are, nevertheless, highly relevant for human societies and ecosystems, and in the context of global warming. We analyzed the well-established $U^{K'}_{37}$ SST proxy, based on the distribution of haptophyte derived alkenones[18], *via* mass spectrometry imaging (MSI)[6] at 100-µm resolution in a 60-cm section of the well-dated core MD03-2621 from the Cariaco Basin. This section spans an age of ~ 11.9 to 11.2 kyr b2k and thus includes the YD-Holocene transition[7]. The resulting SST record provides insights into seasonal to interannual SST variability during the most recent glacial to interglacial transition.

Average reconstructed SST remains relatively stable during the YD-Holocene transition (Fig. 1A), and does not reflect the major environmental change, i.e., the northward shift of the ITCZ expressed in an abrupt change in sediment reflectance (Fig. 1B) and varve thickness[7,15]. At ~11.4 kyr b2k a warming trend is observed: SST increased from an average 23.9 ± 1.6 °C before 11.39 kyr b2k to an average 25.5 ± 1.4 °C after 11.37 kyr b2k. These trends are consistent with conventional $U^{K'}_{37}$ analyses performed in the present study and with those previously reported by Herbert and Schuffert[19] (Extended Data Fig. 1). Three prominent SST maxima are observed between ~11.50 to 11.45 kyr b2k and thus coincide in time with the 11.4 ka cold event, or Preboreal Oscillation (PBO) (Extended Data Fig. 2). The PBO was caused by a weakening of thermohaline circulation[20,21], and is registered in records from Europe and North America as a shift towards dryer, colder conditions[21,22] (Supplementary Information section S1).

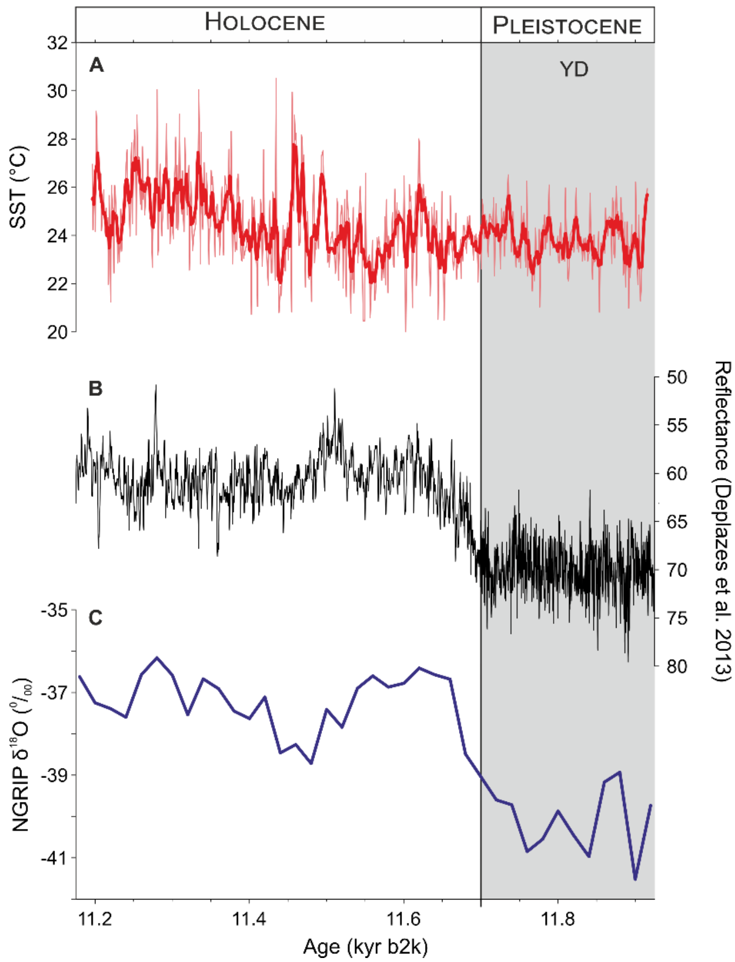

Fig. 1. Reconstructed SST trend in the tropical Cariaco Basin across the YD-Holocene transition based on the $U^{K'}_{37}$ proxy analyzed via MSI. *(**A**) Annually resolved SST (light red line) and 5-yr running average (thick red line). (**B**) Changing sediment reflectance[7] is an indicator of the environmental change in the Cariaco Basin associated to the transition from the cold YD to a milder Holocene, as recorded in (**C**) $\delta^{18}O$ values in Greenland ice cores[9]. Beginning of the Holocene (11.70 kyr b2k) as defined by Rasmussen et al.[9].*

While the longer-term SST trend thus was barely affected during the YD-Holocene transition, short-term variability increased. Frequency analysis of the annually resolved $U^{K'}_{37}$-SST record reveals persistent centennial (120 yr) and multidecadal (42 yr) cycles and significant sub-decadal frequencies that weakened during the latest part of the YD, but became more prominent in the Holocene section (Figure 2 A-C, Extended Data Fig. 3).

We suggest that the weakened interannual variability during the late YD is related to a dampened El Niño-Southern Oscillation (ENSO). ENSO is the strongest mode of climate variability on interannual scales and one of its most robust teleconnections is to SST in the TNA[23,24]. Thereby Pacific El Niño events in boreal fall and winter result in positive SST anomalies the following spring in the TNA. This dependency is modulated by the duration of the ENSO events, more precisely its persistence throughout the late winter, and by the Atlantic multi-decadal oscillation (AMO) phase[25,26]. Located in the western TNA, the Cariaco Basin SST is consequently also driven by the remote influence of ENSO[27]. An updated comparison between ENSO strength and instrumental SST data confirms this relationship (Extended Data Fig. 4).

Climate models have established that during most of the YD, ENSO amplitude was increased compared to the early Holocene[28], driven by the meltwater-induced collapse of overturning circulation[29]. This is consistent with the two available estimations of mid-YD ENSO strength based on individual foraminifera analysis on discrete samples with ages of 12.5 and 12.2 kyr b2k, respectively[30,31]. However, reconstructed minima in ENSO amplitude between 11.68 and 11.86 kyr b2k (Fig 2C, D) in our record suggest that this effect had ceased at least 160 yrs before the Atlantic YD-Holocene transition started, i.e., reorganization in the Pacific climate predated the North Atlantic YD-Holocene transition. Cheng et al.[2] recently claimed that the YD termination might actually have started in the Southern Hemisphere (at ~11.9 kyr) or the tropical Pacific (at ~12.3 kyr), due to a shift from El Niño to La Niña-like conditions. This shift induced a gradual strengthening of AMOC until reaching a tipping point that led to the abrupt rise in North Atlantic temperature. Our Cariaco Basin record supports this hypothesis because of its ability to capture (1) the suggested trigger, i.e., a change in Pacific mean climate state and ocean circulation recorded in the muted ENSO teleconnection during the late YD and (2) the abrupt North Atlantic warming expressed in sediment reflectance data[7] that also resulted in a significant (p=0.006) strengthening of the ENSO amplitude at 11.66 kyr b2k, potentially mediated by continental ice sheet retreat[32] (Fig. 2C, D).

Understanding how the amplitude and frequency of ENSO was forced by climate change in the past is crucial in order to project changes in a warming climate. However, assessing this variability over critical climate transitions (e.g., from glacial to interglacial climate states) through reconstructions or models has proven to be difficult and remains controversial[33,34]. Our record provides a proxy-based, continuous evaluation of ENSO amplitude over the last major event of global warming and confirms its sensitivity to short term forcing.

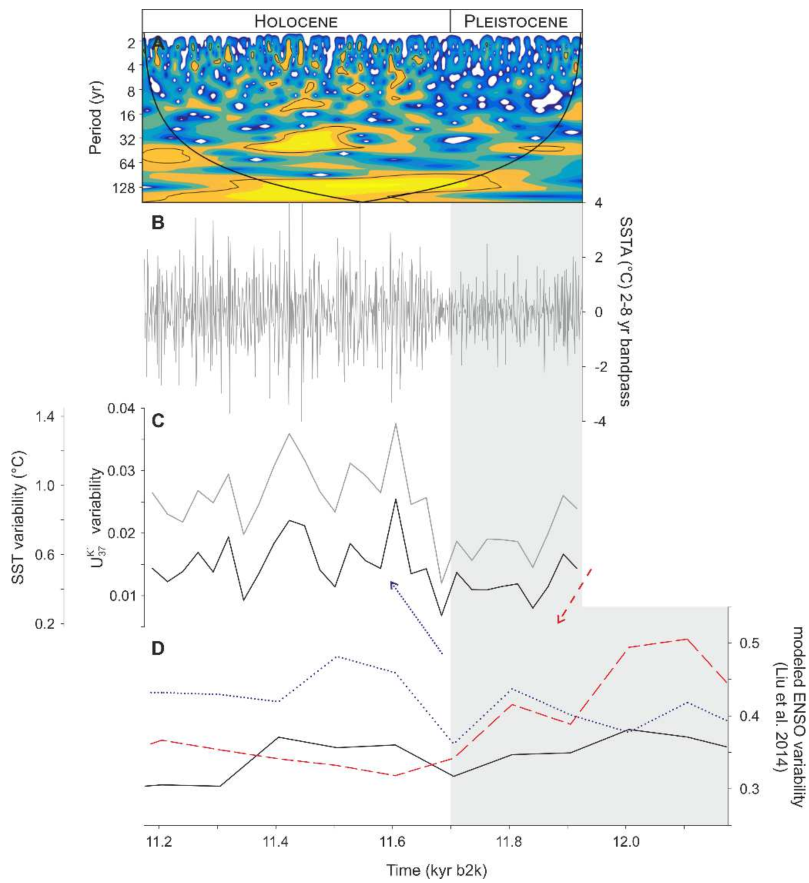

Fig. 2. Interannual SST variability during the YD-Holocene transition. *(**A**) Continuous Morlet wavelet power of the $U^{K'}_{37}$-SST series. Contour lines denote the 95% significance level against red noise, and the thick line marks the cone of influence, (**B**) SST anomaly (SSTA) band-pass-filtered for a period of 2-8 yrs*

and (C) SST variability in the 2-8 yr window for 25 yr intervals. Gray line represents raw data, while the black line shows data corrected for analytical variability (see methods and Supplementary Information section S2). (D) Modeled ENSO amplitude[28] with the complete set of forcings (black line), meltwater discharge forcing (dashed red line) and continental ice sheet forcing (dotted blue line). Red and blue arrows in (C) indicate the proposed effects of meltwater and ice sheet forcing in the Cariaco Basin record.

Subannual SST variability became accessible in our record by deconvoluting the SST signal into upwelling and non-upwelling seasons. This was achieved by combining information on sediment color, elemental composition and $U^{K'}_{37}$ values in each μm-sized spot (Supplementary Information section S3). We confirmed that the investigated laminae couplets represent annual cycles, as already proposed by Hughen et al.[14]: darker layers are enriched in Fe, Ti, and Ca, and correspond to the rainy, non-upwelling (summer/fall) season depositing terrigenous material and biogenic $CaCO_3$ from foraminifera or coccolithophores. Si abundance is highest in lighter layers, and corresponds to the increased biogenic opal production by diatoms during the upwelling (winter/spring) season (Fig. 3B, Extended Data Fig. 5). This blueprint of seasonality was used to assess changes in alkenone abundance (Extended Data Fig. 6) and $U^{K'}_{37}$–based SST reconstruction. Light layers record lower SST values, consistent with upwelling-induced cooling, while darker layers show higher values (Fig. 3C, Extended Data Fig. 7). Deconvolution of reconstructed SST, based on sediment color, enabled us to calculate the seasonality of SST, defined as the difference between average SST in the non-upwelling and the upwelling seasons. SST seasonality significantly strengthened into the Holocene ($p<0.001$). Fitting this increase to a ramp (see methods) results in an abrupt increase from 0.79 to 1.8 °C at 11.64 kyr b2k, while imposing a more gradual increase results in a 160 yr ramp from 0.61 to 1.76 °C (Fig. 3A). Reconstructed early Holocene seasonality is thus very similar to the modern Cariaco Basin (1.6 °C).

This increase in seasonality is concurrent with the change in sediment reflectance, and we therefore posit that it was forced by the position of the ITCZ. As the ITCZ moved northwards, the summer/fall season received larger freshwater input and became less influenced by regional windiness and upwelling[7,12,15]. This scenario presumably allowed the development of density stratification in the water column, with warm surface layers, as opposed to the colder mixed water column of the upwelling season. The incipient strengthening of SST seasonality would have been further supported by a maximum in insolation seasonality over the Cariaco Basin at this time (Extended Data Fig. 8)[35]. In the modern Cariaco Basin, temperature has been identified as a major driver of phytoplankton composition[36], for example exerting a negative effect on most diatoms. Stronger SST seasonality and a warmer non-upwelling season thus can be related to a more pronounced annual succession in the phytoplankton composition and to the shift from a diatom-dominated YD to a coccolithophore-dominated Holocene[16,37].

We further suggest that these changes in seasonality will have impacted previous, lower resolution SST reconstructions and can explain the abrupt warming inferred by Lea et al.[3] (Supplementary Information, section S4). Bova et al.[38] have proposed that climatic events such as the Holocene and Last Interglacial thermal maxima are actually related to seasonal effects, and not to annual SST. Our dataset provides proxy-based evidence of such seasonal effects in the tropics during the last abrupt transition to a warmer climate at the Pleistocene-Holocene boundary.

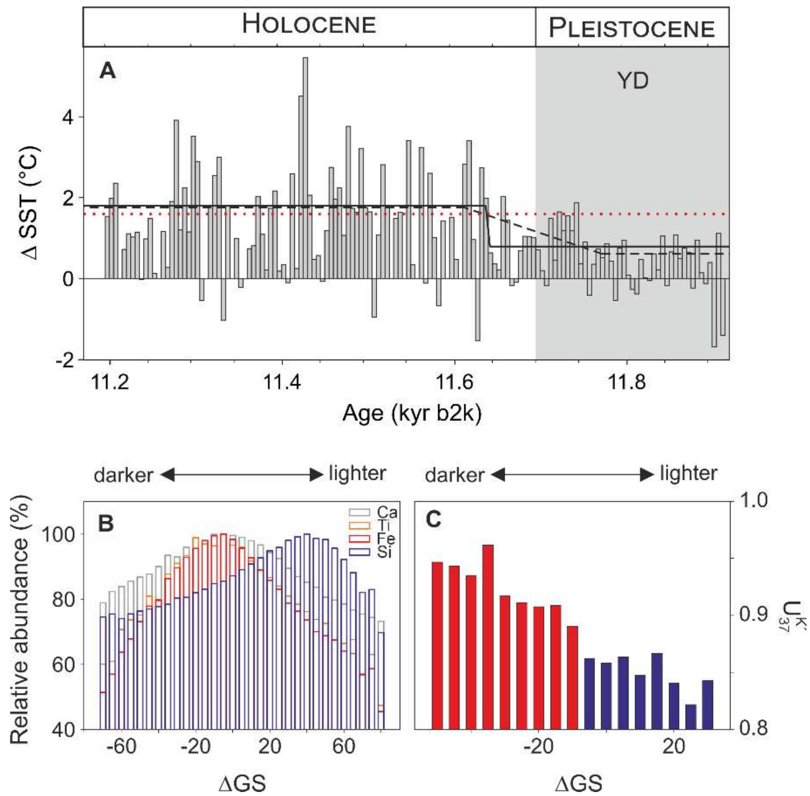

Fig. 3. Reconstructed SST seasonality across the YD-Holocene transition based on the $U_{37}^{K'}$ proxy analyzed via MSI. *(**A**) SST seasonality calculated as the difference between $U_{37}^{K'}$-SST attributed to non-upwelling and upwelling seasons in 5-yr intervals. Increase in Holocene seasonality is fitted to an abrupt and a more gradual ramp (solid and dashed black lines). The red dotted line represents modern Cariaco SST seasonality (1.6 °C). (**B, C**) Seasonality was evaluated by assigning molecular proxy data from each spot to a season of deposition based on sediment color of the spot. (B) Elemental and (C) $U_{37}^{K'}$ data from an exemplary 5-cm slice (490-495 cmbsf, 11.39-11.50 kyr b2k) binned according to sediment color (grayscale, GS). Bins encompassing 5 GS-units and including at least 25 successful $U_{37}^{K'}$ analyses are shown. Red and blue bars in (C) are attributed to non-upwelling and upwelling seasons, respectively. GS is shown as ΔGS, i.e., the difference to the median GS of the whole slice.*

References

1. Shakun, J. D. & Carlson, A. E. A global perspective on Last Glacial Maximum to Holocene climate change. *Quaternary Sci. Rev.* **29**, 1801-1816, doi:10.1016/j.quascirev.2010.03.016 (2010).
2. Cheng, H. *et al.* Timing and structure of the Younger Dryas event and its underlying climate dynamics. *Proc. Natl. Acad. Sci. USA* **117**, 23408-23417, doi:10.1073/pnas.2007869117 (2020).
3. Lea, D. W., Pak, D. K., Peterson, L. C. & Hughen, K. A. Synchroneity of tropical and high-latitude Atlantic temperatures over the last glacial termination. *Science* **301**, 1361-1364, doi:10.1126/science.1088470 (2003).
4. Rühlemann, C., Mulitza, S., Müller, P. J., Wefer, G. & Zahn, R. Warming of the tropical Atlantic Ocean and slowdown of thermohaline circulation during the last deglaciation. *Nature* **402**, 511-514, doi:10.1038/990069 (1999).
5. Alfken, S. *et al.* Mechanistic insights into molecular proxies through comparison of subannually resolved sedimentary records with instrumental water column data in the Santa Barbara Basin, Southern California. *Paleoceanogr. Paleoclimatol.* **35**, e2020PA004076 (2020).
6. Wörmer, L. *et al.* Ultra-high-resolution paleoenvironmental records via direct laser-based analysis of lipid biomarkers in sediment core samples. *Proc. Natl. Acad. Sci. USA* **111**, 15669-15674, doi:10.1073/pnas.1405237111 (2014).
7. Deplazes, G. *et al.* Links between tropical rainfall and North Atlantic climate during the last glacial period. *Nat. Geosci.* **6**, 213-217, doi:10.1038/ngeo1712 (2013).
8. Walker, M. *et al.* Formal definition and dating of the GSSP (Global Stratotype Section and Point) for the base of the Holocene using the Greenland NGRIP ice core, and selected auxiliary records. *J Quaternary Sci* **24**, 3-17, doi:10.1002/jqs.1227 (2009).
9. Rasmussen, S. O. *et al.* A stratigraphic framework for abrupt climatic changes during the Last Glacial period based on three synchronized Greenland ice-core records: refining and extending the INTIMATE event stratigraphy. *Quaternary Sci. Rev.* **106**, 14-28, doi:10.1016/j.quascirev.2014.09.007 (2014).
10. McManus, J. F., Francois, R., Gherardi, J.-M., Keigwin, L. D. & Brown-Leger, S. Collapse and rapid resumption of Atlantic meridional circulation linked to deglacial climate changes. *Nature* **428**, 834-837, doi:10.1038/nature02494 (2004).
11. Broecker, W. S. Paleocean circulation during the last deglaciation: A bipolar seesaw? *Paleoceanogr.* **13**, 119-121, doi:10.1029/97pa03707 (1998).
12. Haug, G. H., Hughen, K. A., Sigman, D. M., Peterson, L. C. & Rohl, U. Southward migration of the intertropical convergence zone through the Holocene. *Science* **293**, 1304-1308, doi:10.1126/science.1059725 (2001).
13. Hughen, K. A., Eglinton, T. I., Xu, L. & Makou, M. Abrupt tropical vegetation response to rapid climate changes. *Science* **304**, 1955-1959, doi:10.1126/science.1092995 (2004).
14. Hughen, K. A., Overpeck, J. T., Peterson, L. C. & Anderson, R. F. The nature of varved sedimentation in the Cariaco Basin, Venezuela, and its palaeoclimatic significance. *Geological Society, London, Special Publications* **116**, 171-183 (1996).
15. Hughen, K. A., Overpeck, J. T., Peterson, L. C. & Trumbore, S. Rapid climate changes in the tropical Atlantic region during the last deglaciation. *Nature* **380**, 51-54, doi:10.1038/380051a0 (1996).
16. Werne, J. P., Hollander, D. J., Lyons, T. W. & Peterson, L. C. Climate-induced variations in productivity and planktonic ecosystem structure from the Younger Dryas to Holocene in the Cariaco Basin, Venezuela. *Paleoceanogr.* **15**, 19-29, doi:10.1029/1998pa000354 (2000).
17. Schmidt, M. W., Spero, H. J. & Lea, D. W. Links between salinity variation in the Caribbean and North Atlantic thermohaline circulation. *Nature* **428**, 160-163, doi:10.1038/nature02346 (2004).
18. Prahl, F. G. & Wakeham, S. G. Calibration of unsaturation patterns in long-chain ketone compositions for paleotemperature assessment. *Nature* **330**, 367-369, doi:10.1038/330367a0 (1987).
19. Herbert, T. D. & Schuffert, J. D. in *Proceedings of the Ocean Drilling Program, Scientific Results.* 239-247.
20. Hald, M. & Hagen, S. Early Preboreal cooling in the Nordic seas region triggered by meltwater. *Geology* **26**, 615-618, doi:10.1130/0091-7613 (1998).
21. Björck, S. *et al.* Synchronized terrestrial-atmospheric deglacial records around the North Atlantic. *Science* **274**, 1155-1160, doi:10.1126/science.274.5290.1155 (1996).
22. Yu, Z. & Eicher, U. Abrupt climate oscillations during the last deglaciation in central North America. *Science* **282**, 2235-2238, doi:10.1126/science.282.5397.2235 (1998).

23 Enfield, D. B. & Mayer, D. A. Tropical Atlantic sea surface temperature variability and its relation to El Niño-Southern Oscillation. *Journal of Geophysical Research: Oceans* **102**, 929-945, doi:10.1029/96JC03296 (1997).

24 Garcia-Serrano, J., Cassou, C., Douville, H., Giannini, A. & Doblas-Reyes, F. J. Revisiting the ENSO Teleconnection to the Tropical North Atlantic. *J. Clim.* **30**, 6945-6957, doi:10.1175/Jcli-D-16-0641.1 (2017).

25 Lee, S. K., Enfield, D. B. & Wang, C. Why do some El Ninos have no impact on tropical North Atlantic SST? *Geophys. Res. Lett.* **35**, doi:10.1029/2008gl034734 (2008).

26 Park, J.-H. & Li, T. Interdecadal modulation of El Niño–tropical North Atlantic teleconnection by the Atlantic multi-decadal oscillation. *Clim. Dynam.* **52**, 5345-5360, doi:10.1007/s00382-018-4452-4 (2019).

27 Astor, Y., Muller-Karger, F. & Scranton, M. I. Seasonal and interannual variation in the hydrography of the Cariaco Basin: implications for basin ventilation. *Cont. Shelf Res.* **23**, 125-144, doi:10.1016/S0278-4343(02)00130-9 (2003).

28 Liu, Z. *et al.* Evolution and forcing mechanisms of El Niño over the past 21,000 years. *Nature* **515**, 550-553, doi:10.1038/nature13963 (2014).

29 Timmermann, A. *et al.* The influence of a weakening of the Atlantic meridional overturning circulation on ENSO. *J. Clim.* **20**, 4899-4919, doi:10.1175/JCLI4283.1 (2007).

30 Sadekov, A. Y. *et al.* Palaeoclimate reconstructions reveal a strong link between El Niño-Southern Oscillation and Tropical Pacific mean state. *Nat Commun* **4**, 1-8, doi:10.1038/ncomms3692 (2013).

31 White, S. M., Ravelo, A. C. & Polissar, P. J. Dampened El Niño in the early and mid-Holocene due to insolation-forced warming/deepening of the thermocline. *Geophys. Res. Lett.* **45**, 316-326, doi:10.1002/2017GL075433 (2018).

32 Lu, Z., Liu, Z. & Zhu, J. Abrupt intensification of ENSO forced by deglacial ice-sheet retreat in CCSM3. *Clim. Dynam.* **46**, 1877-1891, doi:10.1007/s00382-015-2681-3 (2016).

33 Emile-Geay, J., Cobb, K. M., Cole, J. E., Elliot, M. & Zhu, F. in *El Niño Southern Oscillation in a Changing Climate Geophysical Monograph Series* (eds Michael J. McPhaden, Agus Santoso, & Wenju Cai) 87-118 (Wiley-American Geophysical Union, 2020).

34 Zhu, J. *et al.* Reduced ENSO variability at the LGM revealed by an isotope-enabled Earth system model. *Geophys. Res. Lett.* **44**, 6984-6992, doi:10.1002/2017GL073406 (2017).

35 Felis, T. *et al.* Tropical Atlantic temperature seasonality at the end of the last interglacial. *Nat Commun* **6**, 1-8, doi:10.1038/ncomms7159 (2015).

36 Mutshinda, C. M., Troccoli-Ghinaglia, L., Finkel, Z. V., Müller-Karger, F. E. & Irwin, A. J. Environmental control of the dominant phytoplankton in the Cariaco basin: a hierarchical Bayesian approach. *Mar. Biol. Res.* **9**, 246-260, doi:10.1080/17451000.2012.731693 (2013).

37 Dahl, K. A., Repeta, D. J. & Goericke, R. Reconstructing the phytoplankton community of the Cariaco Basin during the Younger Dryas cold event using chlorin steryl esters. *Paleoceanogr.* **19**, doi:10.1029/2003pa000907 (2004).

38 Bova, S., Rosenthal, Y., Liu, Z., Godad, S. P. & Yan, M. Seasonal origin of the thermal maxima at the Holocene and the last interglacial. *Nature* **589**, 548-553, doi:10.1038/s41586-020-03155-x (2021).

Methods

Study site

The Cariaco Basin, located on the continental shelf off Venezuela, is a large (~160 km long and ~65 km wide) depression, composed of two ~1400 m deep sub-basins. It is partially isolated from the Caribbean Sea by a series of sills with depths of less than 150 m[39]. This limits renewal of deep water in the basin and paired with the high oxygen demand resulting from intense surface primary productivity leads to anoxic waters below a depth of currently ~275 m[39,40].

The basin sits within the area of migration of the Atlantic ITCZ, more precisely at its northernmost limit. This translates into a strong seasonal cycle: In summer and fall, heavy precipitation is related to the ITCZ being positioned over the catchment area of the basin and results in intense discharge of continental material by local rivers[41]. In winter and spring, as the ITCZ migrates southward, it allows for strong trade winds, increased upwelling, weakened stratification and highest primary productivity and export of biogenic material[42]. This marked seasonality, combined with anoxic bottom waters that effectively prevents bioturbation, results in the accumulation of varved sediments. As sediments are varved for the last deglaciation and the Holocene, and because of the sensitivity of the area to climate change, they are considered to be one of the most valuable high-resolution marine climate archives, and have been successfully utilized to study climate variability in the tropics[3,7,12-14]. Varve thickness is ~ 1 mm or higher during the Younger Dryas (YD)-Holocene transition[14].

Core and age model

Core MD03-2621 was retrieved during IMAGES cruise XI (PICASSO) aboard R/V Marion Dufresne in 2003. In this study, data from depths between 480 and 540 cm below seafloor are presented, encompassing the YD-Holocene transition. A detailed age model for core MD03-2621 was established by Deplazes et al.[7] and is based on the cross correlation of total reflectance to dated color records from the Cariaco Basin[43,44]. For the studied interval, the original age model is based on a floating varve chronology anchored to tree ring data by matching ^{14}C data[43]. The age model for core MD03-2621 was further fine-tuned by correlation of reflectance data to the NGRIP ice core $\delta^{18}O$ record on the GICC05 age scale[7]. The transition from the Younger Dryas to the Holocene is characterized by a decrease in the sedimentation rate from 1.4 to 0.5 mm yr^{-1}.

To account for possible depth offsets during storage and subsampling, we matched sediment color data expressed as grayscale (GS) to the reflectance data from Deplazes et al.[7] with the software QAnalySeries[45]. To enable comparison to our record, ages in Lea et al.[3] were corrected for the age difference between the sediment color based midpoint of the YD-Holocene transition in their record (11.56 kyr b2k) and in data from Deplazes et al.[7] (11.673 kyr b2k). Start and end of the change in reflectance were determined by the RAMPFIT software[46].

Sample preparation

Samples for MSI of molecular proxies were prepared as described in Alfken et al.[47]: the original core was subsampled by LL channels, from which X-ray pictures (Hewlett-Packard Faxitron 43855A X-ray cabinet) and high-resolution digital images (smart-CIS 1600 Line Scanner) were obtained. The LL channels were then cut into 5-cm pieces, which were subsequently freeze-dried, embedded in a gelatin:carboxymethyl cellulose (4%:1%) mixture, and thin-sectioned on a Microm HM 505E cryomicrotome. From each piece, 60- and 100-µm-thick sediment slices were prepared and affixed to indium tin oxide coated glass slides (Bruker Daltonik, Bremen, Germany) for MSI and elemental mapping, respectively. Slices for MSI were further amended with a fullerite matrix[48].

For all slices, a high-resolution picture was taken on a M4 Tornado system (Bruker Nano Analytics). This picture was used as a reference to set up elemental mapping and MSI analysis, but also for the 2D comparison of elemental and proxy data to sediment color. Sediment color is expressed as GS value. To account for differences between single slices, ΔGS was calculated as the difference between a value and the median GS of each individual slice. Very low GS values corresponding to areas devoid of sediment, identified by a black background, were excluded from analysis.

Elemental mapping

Elemental mapping of 100 µm-thick slices was performed on a M4 Tornado system (Bruker Nano Analytics) equipped with a micro-focused Rh source (50 kV, 600 µA) with a poly-capillary optic. Measurements were conducted under vacuum, with a resolution of 50 µm, 2 scans per spot and a scan time of 5 ms per scan. Data were initially processed and visualized with M4 Tornado Software version 1.3. xy-matrices of relevant elements and sediment color were afterwards imported into Matlab (R2016b) for further processing. To assess the correspondence between sediment color and elemental composition, for each 5-cm piece signal intensities of Ca, Fe, Ti and Si in single spots were binned according to ΔGS, and average intensities were calculated for each bin. Bin size was 5 units.

Molecular proxy analysis by MSI

MSI was carried out on a 7T solariX XR FT-ICR-MS coupled to a MALDI source equipped with a Smartbeam II laser (Bruker Daltonik, Bremen, Germany). Analyses were performed in positive ionization mode selecting for a continuous accumulation of selective ions (CASI) window of *m*/*z* 554 ± 12. Spectra were acquired with 25% data reduction to limit data size. Spatial resolution was obtained by rastering the ionizing laser across the sample in a defined rectangular area at a

100 µm spot distance. Considering laminae thickness in the millimeter range[14], such raster resolution is suited for seasonally resolved SST reconstruction. Settings for laser power, frequency and number of shots were adjusted for optimal signal intensities before each measurement, typical values were 250 shots with 200 Hz frequency and 60% laser power. External mass calibration was performed in electrospray ionization mode with sodium trifluoroacetate (Sigma Aldrich). Each spectrum was additionally calibrated after data acquisition by an internal lock mass calibration using the Na^+ adduct of pyropheophorbide *a* (*m/z* 557.2523), a chlorophyll *a* derivative generally present in relatively young marine sediments. Around 20.000 individual spots were thereby obtained for every 5-cm sample, each spot containing information on the abundance of di- and triunsaturated C_{37} alkenones needed to calculate the $U^{K'}_{37}$ sea surface temperature (SST) proxy.

We provide a two-pronged approach to decode SST proxy information: (i) a downcore $U^{K'}_{37}$ profile was obtained by pooling alkenone data from coeval horizons, and results in SST reconstructions with annual resolution, and (ii) 2D images of proxy distribution were examined in conjunction with maps of sediment color and elemental distribution to filter single-spot proxy data for season of proxy deposition.

SST reconstruction with yearly resolution

For the downcore profile, MSI data were referenced to the X-ray image by the identification of three teaching points per 5-cm piece. Afterwards, the X-ray image was corrected for tilting of laminae as described in Alfken et al.[5]. After applying the corresponding age model, downcore profiles were established with 1-yr resolution: Intensity of the two alkenone species relevant to the $U^{K'}_{37}$ proxy ($C_{37:2}$ and $C_{37:3}$) were recorded for each individual laser spot and filtered for a signal-to-noise threshold of 3. Only spots in which both compounds were detected were further considered. Intensity values were then summed up over the depth corresponding to one year. By pooling proxy data into 1-yr horizons, the effect of changing sedimentation rate and thereby changing downcore resolution is minimized. If at least ten spots presenting both compounds were available for a single horizon, data quality criteria were satisfied[48] and a $U^{K'}_{37}$ value was calculated as defined by Prahl and Wakeham [18]:

$$U^{K'}_{37} = \frac{C_{37:2}}{C_{37:2} + C_{37:3}} \text{ (equation 1)}$$

In order to apply the GC-based calibrations for the $U^{K'}_{37}$ proxy, MSI-based data were converted to GC equivalents. Therefore, after MSI, sediment slices were extracted for conventional proxy analysis. Sediment was scraped off the slide and extracted following a modified Bligh & Dyer procedure[49,50]. Extracts were evaporated under a stream of nitrogen, re-dissolved in n-hexane and analyzed on a ThermoFinnigan Trace GC-FID equipped with Restek Rxi-5ms capillary column (30 m × 0.25 mm ID). For each 5-cm piece a ratio between the $U^{K'}_{37}$ values obtained by GC-FID analysis and MSI was calculated. The average ratio of all pieces for which GC-based values could be obtained was 1.194, with a standard deviation of 0.021.

$$U^{K'}_{37\ GC-FID} = 1.194 \times U^{K'}_{37\ MSI} \text{ (equation 2)}$$

This ratio was used to calculate GC-equivalent $U^{K'}_{37}$ values, which were then translated into SST using the BAYSPLINE calibration[51]. According to Alfken et al.[5], analytical precision of MSI-based SST reconstructions using at least ten data points for the $U^{K'}_{37}$ is ~0.3 °C.

For frequency analysis, a continuous, annually-spaced record was constructed by linearly interpolating 49 missing values. The record was subsequently detrended. Spectral analysis was performed with the REDFIT module[52] using a Hanning windows (oversample 2, segments 2). Continuous wavelet transforms were applied to investigate changes in cyclicity across time, using the Morlet wavelet with code provided by Torrence and Compo[53] for Matlab. All steps, except for the wavelet analysis, were performed with the PAST software[54].

For the assessment of the variability attributed to ENSO, the SST record was band-pass filtered for periods between 2 and 8 yrs. As described above, the record is based on 1-yr binned data, seasonality is thereby nullified and the highest frequency to be evaluated (Nyquist frequency) corresponds to a period of 2 years. Variability of this time series was quantified by calculating the standard deviation of the band-pass filtered $U^{K'}_{37}$ signal in 25 yr-intervals. To account for the potential impact of analytical precision on the observed signal (Supplementary Information section S2), the variability experiment from Alfken et al.[5] was revisited. A sediment extract had been sprayed on an ITO slide and analyzed by MSI. We then randomly selected *n* spots and obtained a $U^{K'}_{37}$ value for the summed intensities of these spots. Precision was calculated as the standard deviation of 5 replicate experiments for *n*=1, 5, 10, 20, 30, 40, 50, 60. Decreasing analytical variability with increasing number of observations was fitted to a curve (R^2=0.838) described by the equation

$$Analytical\ variability\ = 0.0741 \times number\ of\ spots^{-0.558}$$ (equation3)

Based on this equation, analytical variability for each horizon could be calculated based on the number of values included. Mean variability for each 25-yr window was then subtracted from the observed variability in the band-pass filtered signal and the resulting proxy values were translated to SST following the equation by Müller et al.[55]. Statistical significance of the change in corrected SST variability after 11.66 kyr b2k was assessed with a t-test.

Assessment of SST seasonality

For the assessment of SST seasonality, alkenone intensities from individual spots were binned according to ΔGS, with a bin size of 1 unit. Spots were then separated into the categories upwelling and non-upwelling season by identifying the threshold ΔGS value that maximized the difference between average SST in the bins above and below it. Additionally, this value had to fulfill three conditions: (a) be higher (lighter) than the bin with the highest relative abundance of Ca, Ti and Fe, indicative of the dark sediments associated to the non-upwelling season (b) be lower (darker) than the bin with highest relative abundance for Si, indicative of light sediment associated to the upwelling season and (c) the number of spots categorized as upwelling and non-upwelling had to account for at least 25% of total spots. If criteria 1 and 2 prevented criteria 3 from being fulfilled, a limit of 15% was set. After separating data into these two categories, data were processed separately as described above for the unfiltered dataset, and a downcore temporal resolution of 5 years was applied. Seasonality was calculated as the difference between both records and thus represents the difference between 5-yr average SST in the non-upwelling and upwelling seasons.

Shift in seasonality was fitted to two different ramps with the RAMPFIT software[46]. An unconstrained approach and a constrained approach (in which start and end-points of the ramp were restricted to the intervals 11.725-11.8 kyr b2k and 11.6-11.675 kyr b2k) were applied. Negative values were excluded from this fitting. Resulting group of data were compared by a Mann Whitney Rank test.

SST seasonality in the modern Cariaco Basin was calculated for the years 1980 to 2020 based on the HadISST data set[56] by dividing monthly data from each year into two groups and searching for the largest difference between average temperatures of both groups. Each group had to include at least 3 consecutive months. In 36 out of 41 years, the warm season was defined from May to November or from July to November.

Methods References

39 Richards, F. A. & Vaccaro, R. F. The Cariaco Trench, an anaerobic basin in the Caribbean Sea. *Deep-Sea Res* **3**, 214-228, doi:10.1016/0146-6313(56)90005-3 (1956).

40 Thunell, R. C. *et al.* Organic carbon fluxes, degradation, and accumulation in an anoxic basin: Sediment trap results from the Cariaco Basin. *Limnol. Oceanogr.* **45**, 300-308, doi:10.4319/lo.2000.45.2.0300 (2000).

41 Elmore, A. C. *et al.* Quantifying the seasonal variations in fluvial and eolian sources of terrigenous material to Cariaco Basin, Venezuela. *J. S. Am. Earth Sci.* **27**, 197-210, doi:10.1016/j.jsames.2008.11.002 (2009).

42 Montes, E. *et al.* Vertical fluxes of particulate biogenic material through the euphotic and twilight zones in the Cariaco Basin, Venezuela. *Deep-Sea Res. Pt. I* **67**, 73-84, doi:10.1016/j.dsr.2012.05.005 (2012).

43 Hughen, K. A., Southon, J. R., Bertrand, C. J. H., Frantz, B. & Zermeno, P. Cariaco basin calibration update: Revisions to calendar and C-14 chronologies for core PL07-58PC. *Radiocarbon* **46**, 1161-1187, doi:10.1017/S0033822200033075 (2004).

44 Hughen, K., Southon, J., Lehman, S., Bertrand, C. & Turnbull, J. Marine-derived ^{14}C calibration and activity record for the past 50,000 years updated from the Cariaco Basin. *Quaternary Sci. Rev.* **25**, 3216-3227, doi:10.1016/j.quascirev.2006.03.014 (2006).

45 Kotov, S. & Paelike, H. QAnalySeries - a cross-platform time series tuning and analysis tool. *AGU 2018 Fall Meeting* **2018**, PP53D-1230 (2018).

46 Mudelsee, M. Ramp function regression: a tool for quantifying climate transitions. *Comput. Geosci.* **26**, 293-307, doi:10.1016/S0098-3004(99)00141-7 (2000).

47 Alfken, S. *et al.* Micrometer scale imaging of sedimentary climate archives - Sample preparation for combined elemental and lipid biomarker analysis. *Org. Geochem.* **127**, 81-91, doi:10.1016/j.orggeochem.2018.11.002 (2019).

48 Wörmer, L. *et al.* Towards multiproxy, ultra-high resolution molecular stratigraphy: Enabling laser-induced mass spectrometry imaging of diverse molecular biomarkers in sediments. *Org. Geochem.* **127**, 136-145, doi:10.1016/j.orggeochem.2018.11.009 (2019).

49 Bligh, E. G. & Dyer, W. J. A rapid method of total lipid extraction and purification. *Can. J. Biochem. Phys.* **37**, 911-917, doi:10.1139/o59-099 (1959).

50 Wörmer, L., Lipp, J. S. & Hinrichs, K.-U. in *Hydrocarbon and Lipid Microbiology Protocols: Petroleum, Hydrocarbon and Lipid Analysis* (eds Terry J. McGenity, Kenneth N. Timmis, & Balbina Nogales) 289-317 (Springer Berlin Heidelberg, 2017).

51 Tierney, J. E. & Tingley, M. P. BAYSPLINE: A new calibration for the alkenone paleothermometer. *Paleoceanogr. Paleoclimatol.* **33**, 281-301, doi:10.1002/2017PA003201 (2018).

52 Schulz, M. & Mudelsee, M. REDFIT: estimating red-noise spectra directly from unevenly spaced paleoclimatic time series. *Comput. Geosci.* **28**, 421-426, doi:10.1016/s0098-3004(01)00044-9 (2002).

53 Torrence, C. & Compo, G. P. A practical guide to wavelet analysis. *B. Am. Meteorol. Soc.* **79**, 61-78, doi:10.1175/1520-0477 (1998).

54 Hammer, O., Harper, D. A. T. & Ryan, P. D. PAST: paleontological statistics software package for education and data analysis. *Palaeontologia Electronica* **4** (2001).

55 Müller, P. J., Kirst, G., Ruhland, G., von Storch, I. & Rosell-Mele, A. Calibration of the alkenone paleotemperature index $U_{37}^{K'}$ based on core-tops from the eastern South Atlantic and the global ocean (60 degrees N-60 degrees S). *Geochim. Cosmochim. Acta* **62**, 1757-1772, doi:10.1016/s0016-7037(98)00097-0 (1998).

56 Rayner, N. *et al.* Global analyses of sea surface temperature, sea ice, and night marine air temperature since the late nineteenth century. *J. Geophys. Res.-Atmos.* **108**, doi:10.1029/2002JD002670 (2003).

Data availability: Data are accessible in the Pangaea database under doi:### (will be updated during revision)

Acknowledgments: We thank Susanne Alfken, Tiffany Napier, Igor Obreht and Jürgen Pätzold for fruitful discussions and comments to an earlier draft, and Zhengyao Lu for sharing data on modeled ENSO variability. This research was supported by the European Research Council under the European Union's Horizon 2020 Research and Innovation Programme, grant agreement No. 670115 ZOOMECULAR (K.-U. H.) and by Germany's Excellence Strategy (EXC-2077) project 390741603 "The Ocean Floor – Earth's Uncharted Interface".

Author contributions:

Conceptualization: LW, GH, K-UH, Methodology: LW, JW, Software: LW, BB, Formal Analysis: LW, Investigation: LW, JW, BB, Resources: GH, K-UH, Writing-Original Draft: LW, K-UH, Writing-Review & Editing: LW, BB, GH, K-UH, Visualization: LW, Funding Acquisition: LW, K-UH

Competing interests: Authors declare that they have no competing interests.

Additional Information: Supplementary Information is available for this paper.

Extended Data Figures 1-10.

Supplementary Files

This is a list of supplementary files associated with this preprint. Click to download.

- WoXXrmeretalCariacoSupplementaryExtendedData2.pdf